Methods

Animals

We studied 5 goats (70.4 ± 14.71 kg) with acute LV dysfunction because of coronary microsphere embolization, and 5 goats with normal hearts (58.3 ± 7.59 kg). The animals used in this study were maintained in accordance with the guidelines of the Committee on Animal Studies at the National Cerebral and Cardiovascular Center. This study was approved by the National Cerebral and Cardiovascular Center Animal Investigation Committee.

Surgical procedures, implanted devices

Animals were tranquilized with ketamine hydrochloride (8–10 mg/kg im) and anesthetized with isoflurane (1–3 vol/100 mL in oxygen). After being draped and prepped in the right lateral recumbent position, they were intubated and mechanically ventilated. A left thoracotomy was performed and the fifth costal bone was resected. We approached the heart through the left thoracic space. We retained the left intra-thoracic artery and vein, to enable measurement of aortic pressure (AoP) and venous pressure (CVP), and also to obtain blood gas analysis data. The blood flow rates of the ascending aorta, LVAD, and coronary artery (the left main trunk, LMT) were measured by use of flow meters. We used an electromagnetic flow meter (EMF-1000: 16–22 mm in diameter; Nihon Kohden, Tokyo, Japan) for the aorta, an ultrasonic flow meter (HQD3FSB: 3–4 mm; Transonic Systems, NY, USA) for the LMT, and an ultrasonic flow meter (TS420: 16 mm; Transonic Systems) for the LVAD. After heparinization (300 U/kg), the centrifugal LVAD (EVAHEART®; Sun Medical Technology Research Corporation, Nagano, Japan) was installed, by inserting the inflow cannula into the left ventricular apex and suturing the outflow conduit to the descending aorta. A 6 Fr conductance catheter (2S-RH-6DA-116, Taisho Biomed Instrument, Osaka, Japan) and a 4 Fr micro-tip catheter pressure transducer (Millar Instruments, Houston, TX, USA) were inserted into the left ventricle from the anterior wall, for the purpose of obtaining data for the pressure–volume curve of the left ventricle. Blood gas analysis of the coronary vein was performed using data obtained from a catheter inserted into the accessory hemiazygos vein, which runs to the coronary vein in goats. The vital data mentioned above were recorded by use of Labchart 5 software (ADInstruments, Castle Hill, Australia). The pressure and volume data of the LV were recorded by use of a Leycom Sigma 5 (CardioDynamics, Zoetermeer, The Netherlands).

LV dysfunction model

To create a model of acute LV dysfunction, we embolized the left anterior descending coronary artery (LAD) as described elsewhere [9–11]. A multipurpose Judkins catheter (4 Fr) was introduced through a long sheath (4 Fr × 17 cm) into the left carotid artery toward the LAD with fluoroscopic guidance. We then injected the microspheres (size 50 μm, 10,000/kg) into the LAD. After observation for 10 min we added more microsphere (5,000/kg), because the aortic flow (AoF) was more than 60% of the preoperative AoF. Total amount was 0.66 ± 0.227 million. The general condition was observed for 30 additional minutes before data collection to stabilize and optimize cardiac function.

Study protocol and LVAD control

We controlled the AoP and CVP to achieve a stable condition during the examination, so as not to change the afterload and preload of the heart. We controlled the heart rate by adjusting the volume of transfusion and changing the depth of anesthesia, but did not infuse either a vasodilator or catecholamine. We used 2% lidocaine (1 mg/kg/h) and nifekalant hydrochloride (0.4 mg/kg/h) during the experiment to prevent ventricular arrhythmia.

We have already reported details of our novel pump controller, which can change the RS of the EVAHEART® so it is synchronized with the cardiac cycle [7, 8, 12, 13]. We defined the systolic phase as 33% of the RR interval and the diastolic phase as 67% of the RR interval, and input the duration of each phase in accordance with the heart rate. Our controller can change the RS of each phase, detecting the R wave from the ECG. The BR was calculated by dividing the pump flow (PF) rate by the sum of the pump and AoF rate.

Using this controller, we compared 4 driving modes in this study. The first was the "circuit clamp (pump off)" mode, clamping the LVAD circuit to evaluate the conditions of a native heart. The next was the "continuous" mode, driving the LVAD continuously with a stable rotation speed. This is the mode, we usually use clinically. The third was the "counter-pulse" mode. In this driving mode, we set the RS of the systolic phase to approximately 700 rpm, the minimum speed of LVAD system, and adjusted the RS of the diastolic phase to achieve a proper BR as needed. In this study, the BR was set to be 100%, and 80–120% was allowed. The last mode was the "co-pulse mode". This mode is defined as the opposite of the counter-pulse mode. In this driving mode, we set the RS of the diastolic phase to approximately 1,000 rpm, so as not to induce reversed flow inside the LVAD circuit, and adjusted the RS of the systolic phase to achieve a BR of 100%.

We acquired all data 5 min after setting each mode. This period was considered sufficient for stabilization of the conditions. In this study, we mainly evaluated the EDV of the left ventricle.

Results

Sample waveforms of the ECG, AoP, CVP, LV pressure (LVP), PF, AoF, CoF, RS, and BR are shown in Fig. 1. In the counter-pulse mode, increased RS reduced the amplitude of the waveforms of AoP and PF in the diastolic phase. The amount of CoF in the diastolic phase was increased in this mode compared with that in the other modes. In the co-pulse mode, increased RS sharpened the waveforms of AoP and PF in the systolic phase. The reversed flow through the LVAD was equivalent to the PF wave below zero line in the diastolic phase. It was larger than in any other modes. BR was not significantly different in any of the modes except circuit-clamp.

Hemodynamic data for the normal and acute heart-failure models in each mode are shown in Table 1. Heart rate, CVP, AoP, amount of total flow, and bypass rate were not significantly different among the modes.

Figure 2 shows echocardiographic images from the left ventricle in the end-diastolic phase. The upper chamber is the left ventricle. The outflow cannula was inserted from the apex (shown in the left side of picture). The size of the

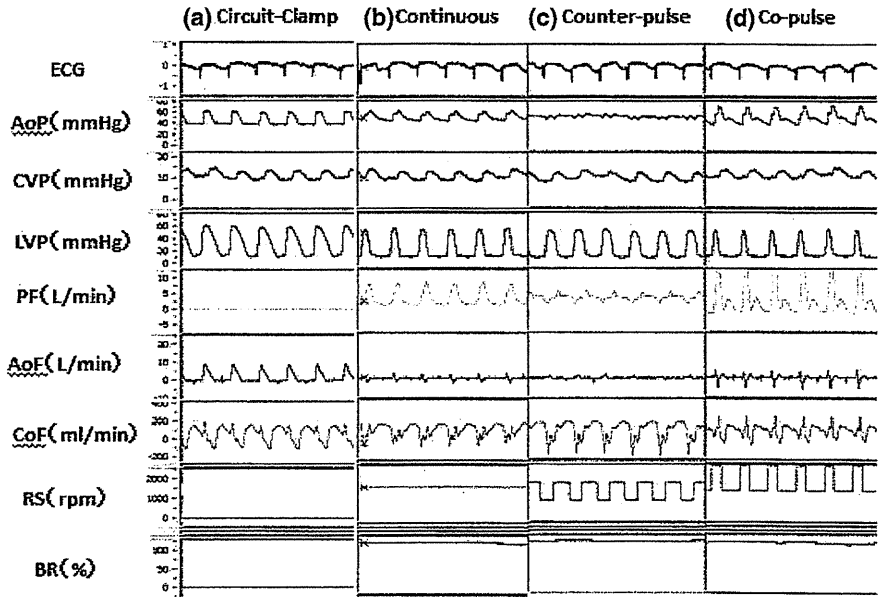

Fig. 1 Waveforms of pressure and flow. *PF* pump flow, *AoF* ascending aortic flow, *CoF* coronary flow, *RS* rotational speed, *BR* bypass rate. In the counter-pulse mode, increased RS reduced the amplitude of the waveforms of AoP and PF in the diastolic phase. In the co-pulse mode, increased RS sharpened the waveforms of AoP and PF in the systolic phase

Table 1 Hemodynamic data for normal and acute ischemic models in each mode

	Circuit-clamp	Continuous	Counter-pulse	Co-pulse
Normal heart				
HR (rpm)	79.6 ± 6.3	83.4 ± 18.3	76.8 ± 5.4	77.3 ± 6.3
Mean CVP (mmHg)	10.5 ± 2.7	10.3 ± 3.0	10.2 ± 2.9	10.3 ± 2.9
Mean AoP (mmHg)	58.7 ± 7.3	63.6 ± 8.3	60.2 ± 7.8	58.0 ± 7.3
Pump flow (L/min)	0.0 ± 0.0	3.13 ± 0.60	2.87 ± 0.33	2.81 ± 0.37
Total flow (L/min)	3.64 ± 0.97	3.38 ± 0.97	3.44 ± 0.98	3.20 ± 0.96
Bypass rate (%)	0.0 ± 0.0	91.2 ± 12.6	90.5 ± 15.3	90.4 ± 13.0
Heart failure				
HR (rpm)	77.7 ± 13.2	77.0 ± 12.4	71.8 ± 15.9	72.2 ± 16.4
Mean CVP (mmHg)	16.9 ± 7.0	16.4 ± 5.9	16.9 ± 6.0	17.0 ± 6.2
Mean AoP (mmHg)	58.9 ± 18.2	59.2 ± 11.1	58.6 ± 9.7	54.9 ± 5.7
Pump flow (L/min)	0.0 ± 0.0	3.08 ± 1.31	2.58 ± 1.04	2.48 ± 1.02
Total flow (L/min)	2.40 ± 1.07	2.82 ± 1.11	2.55 ± 1.23	2.39 ± 1.11
Bypass rate (%)	0.0 ± 0.0	109.0 ± 14.2	107.9 ± 28.1	107.5 ± 22.3

Heart rate, CVP, AoP, amount of total flow, and bypass rate were not significantly different among the modes

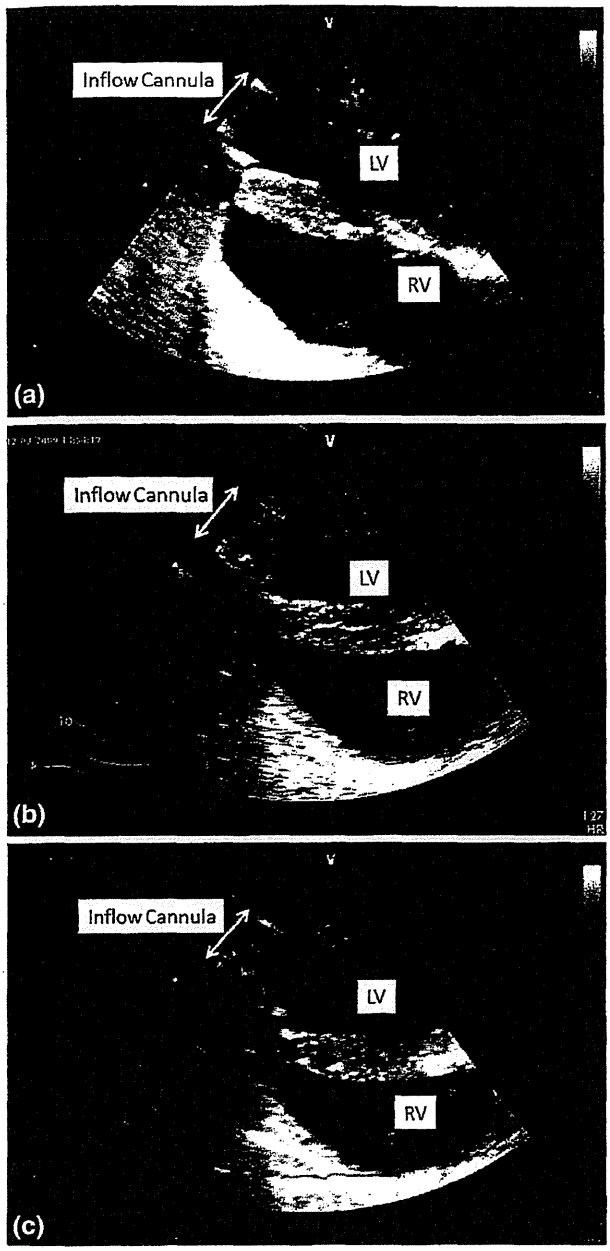

Fig. 2 Echocardiography of the end-diastolic phase (**a** continuous mode, **b** counter-pulse mode, **c** co-pulse mode). The size of the left ventricle was significantly reduced in the counter-pulse mode (**b**) and increased in the co-pulse mode (**c**) compared with that in the continuous mode (**a**)

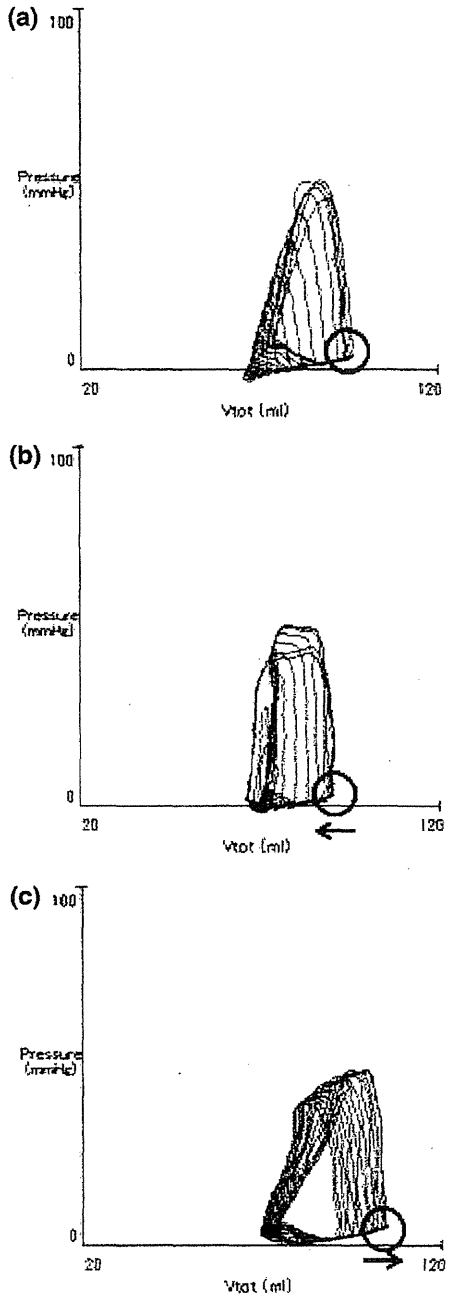

Fig. 3 Pressure–volume loops in the continuous mode (**a**), counter-pulse mode (**b**), and co-pulse mode (**c**) for the acute heart-failure model. The left ventricular end-diastolic volume (EDV) was increased in the co-pulse mode (shift to the right) and reduced in the counter-pulse mode (shift to the left)

left ventricle was significantly reduced in the counter-pulse mode (Fig. 2b) and increased in the co-pulse mode (Fig. 2c) compared with that in the continuous mode (Fig. 2a).

Pressure–volume curves for the left ventricle in the each mode for the acute heart-failure model are shown in Fig. 3. The vertical axis expresses the left ventricular pressure and the horizontal axis expresses the left ventricular volume. The left ventricular EDV was increased in the co-pulse mode (shift to the right) and reduced in the counter-pulse mode (shift to the left).

Figure 4 shows the EDV for each mode, as a percentage of that for the circuit clamp mode (= 100%). The LV EDV decreased in the counter-pulse mode and increased in the

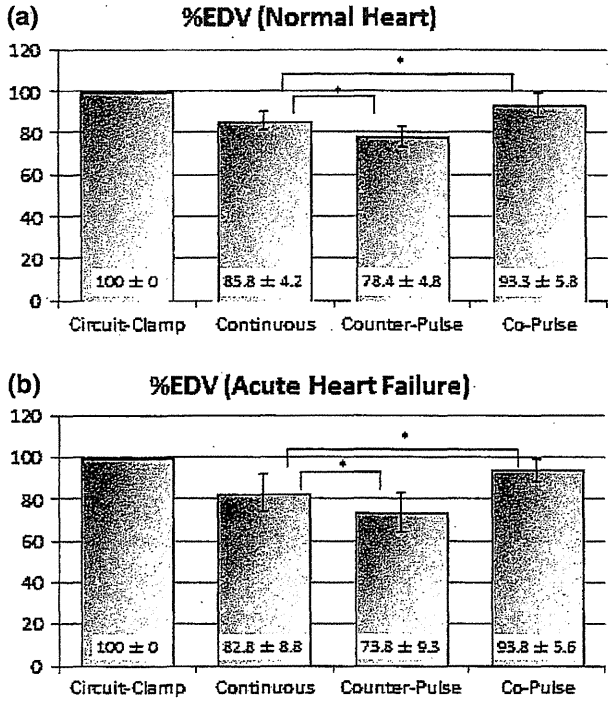

Fig. 4 LV end-diastolic volume in the different modes (circuit-clamp = 100%). The LV end-diastolic volume decreased in the counter-pulse mode and increased in the co-pulse mode, compared with the continuous mode ($p < 0.05$), in both the normal (**a**) and acute heart-failure models (**b**)

co-pulse mode, compared with the continuous mode ($p < 0.05$), in both normal and acute heart-failure models. As a percentage of that in the circuit clamp mode (100%), EDV was 78.4 ± 4.8% in the counter-pulse mode, 93.3 ± 5.8% in the co-pulse mode, and 85.8 ± 4.2% in the 100% continuous support mode, for the normal heart. The same trend was also detected in the acute ischemic heart, where EDV was 73.8 ± 9.3% in the counter-pulse mode, 93.8 ± 5.6% in the co-pulse mode, and 82.8 ± 8.8% in the continuous support mode.

Discussion

We developed a novel drive mode to improve the quality of life of patients with continuous-flow LVAD, a group which is currently expanding rapidly. Our primary objective was to improve the function of the native heart as much as possible by developing a new operating method for the LVAD. In this study, we focused on the left ventricular EDV, which we expect to control with the continuous-flow LVAD by use of the pulsatile driving technique. EDV is considered to be a one of the factors which determine the native heart load. According to Frank–Starling's law of the heart, external work against afterload depends on the EDV. The pressure–volume area (PVA) is defined as the area framed by the lines of the end-diastolic and systolic pressure–volume relationship and the pressure–volume curve of the systolic phase. PVA is believed to be equivalent to the sum of external work and potential energy. Furthermore, it is known to have a direct correlation with myocardial oxygen consumption [14–16].

Usually, EDV is reduced in size with continuous LVAD [17–20], so LVAD implantation therapy affects LV volume reduction. With our novel LVAD driving technique, however, we can change the EDV as we like. This result means it may be possible to control the native heart load with the continuous-flow LVAD. We can give more support to the native heart, by reducing its load with the counter-pulse mode, when we need to for severe heart-failure patients. In contrast, we can apply more over load to the native heart by increasing its load with the co-pulse mode, when we want to train the native heart to wean it from the LVAD. With this novel driving method, we may have great opportunities to make good use of the continuous LVAD, according to the native heart condition.

Additionally, the large EDV of the co-pulse mode may be useful for preventing a critical complication, thrombosis. Recently, thrombosis has been well controlled by whole body management including anticoagulation, but it is still a critical complication for patients with LVAD. One reason for this complication is believed to be the wedge thrombus which is likely to be formed in the space between the left ventricular muscle and the inflow cannula of the LVAD. If EDV becomes larger in the co-pulse mode, blood flow may wash out this space and prevent the formation of a wedge thrombus. As a result, the co-pulse mode may enable this thrombosis to be avoided. If we use this mode, however, we should take into consideration the resulting load on the heart, as mentioned above.

In this report, we evaluate our novel LVAD driving technique from the aspect of the EDV only. We are now in the process of evaluating this method from the aspects of myocardial oxygen consumption, the LV PVA, and the amount of CoF, with a variety of BRs. Furthermore we are now developing chronic heart-failure models, because we also wish to evaluate this method with such models. Such analysis may result in great benefits to patients with chronic heart failure.

Conclusion

Our experiment using goats with normal and acute ischemic hearts showed that EDV was smaller in the counter-pulse mode and larger in the co-pulse mode, than in the continuous support mode, which we usually use clinically. This result means it may be possible to achieve a favorable

EDV and native heart load by controlling the rotation of continuous-flow LVAD so it is synchronized with the cardiac beat. This novel driving system may be of great benefit to patients with end-stage heart failure, especially those with ischemic etiology.

References

1. Potapov EV, Loebe M, Abdul-Khaliq H, Koster A, Stein J, Sodian R, Kopitz M, Hausmann H, Noon GP, DeBakey ME, Hetzer R. Postoperative course of S-100B protein and neuron-specific enolase in patients after implantation of continuous and pulsatile flow LVADs. J Heart Lung Transplant. 2001;20:1310–6.
2. Zimpfer D, Wieselthaler G, Czerny M, Fakin R, Haider D, Zrunek P, Roethy W, Schima H, Wolner E, Grimm M. Neurocognitive function in patients with ventricular assist devices: a comparison of pulsatile and continuous blood flow devices. ASAIO J. 2006;52:24–7.
3. Koenig SC, Pantalos GM, Gillars KJ, Ewert DL, Litwak KN, Etoch SW. Hemodynamic and pressure–volume responses to continuous and pulsatile ventricular assist in an adult mock circulation. ASAIO J. 2004;50:15–24.
4. Garatti A, Bruschi G, Colombo T, Russo C, Lanfranconi M, Milazzo F, Frigerio M, Vitali E. Clinical outcome and bridge to transplant rate of left ventricular assist device recipient patients: comparison between continuous-flow and pulsatile-flow devices. Eur J Cardiothorac Surg. 2008;34:275–80. discussion 280. Epub 2008 Mar 28.
5. Yamazaki K, Kihara S, Akimoto T, Tagusari O, Kawai A, Umezu M, Tomioka J, Kormos RL, Griffith BP, Kurosawa H. EVAHEART: an implantable centrifugal blood pump for long-term circulatory support. J Thorac Cardiovasc Surg. 2002;50:461–5.
6. Yamazaki K, Saito S, Kihara S, Tagusari O, Kurosawa H. Completely pulsatile high flow circulatory support with a constant-speed centrifugal blood pump: mechanisms and early clinical observations. Thorac Cardiovasc Surg. 2007;55:158–62.
7. Ando M, Nishimura T, Takewa Y, Yamazaki K, Kyo S, Ono M, Tsukiya T, Mizuno T, Taenaka Y, Tatsumi E. Electrocardiogram-synchronized rotational speed change mode in rotary pumps could improve pulsatility. Artif Organs. 2011;35:941–7.
8. Ando M, Takewa Y, Nishimura T, Yamazaki K, Kyo S, Ono M, Tsukiya T, Mizuno T, Taenaka Y, Tatsumi E. A novel counterpulsation mode of rotary left ventricular assist devices can enhance myocardial perfusion. J Artif Organs. 2011;14:185–91.
9. Klocke R, Tian W, Kuhlmann MT, Nikol S. Surgical animal models of heart failure related to coronary heart disease. Cardiovasc Res. 2007;74:29–38.
10. Dixon JA, Spinale FG. Large animal models of heart failure: a critical link in the translation of basic science to clinical practice. Circ Heart Fail. 2009;2:262–71.
11. Gill RM, Jones BD, Corbly AK, Wang J, Braz JC, Sandusky GE, Wang J, Shen W. Cardiac diastolic dysfunction in conscious dogs with heart failure induced by chronic coronary microembolization. Am J Physiol Heart Circ Physiol. 2006;291:H3154–8.
12. Ando M, Nishimura T, Takewa Y, Ogawa D, Yamazaki K, Kashiwa K, Kyo S, Ono M, Taenaka Y, Tatsumi E. What is the ideal off-test trial for continuous-flow ventricular-assist-device explantation? Intracircuit back-flow analysis in a mock circulation model. J Artif Organs. 2011;14:70–3.
13. Ando M, Nishimura T, Takewa Y, Ogawa D, Yamazaki K, Kashiwa K, Kyo S, Ono M, Taenaka Y, Tatsumi E. A novel counterpulse drive mode of continuous-flow left ventricular assist devices can minimize intracircuit backward flow during pump weaning. J Artif Organs. 2011;14:74–9.
14. Suga H. Total mechanical energy of a ventricle model and cardiac oxygen consumption. Am J Physiol. 1979;236:H498–505.
15. Suga H, Igarashi Y, Yamada O, Goto Y. Cardiac oxygen consumption and systolic pressure volume area. Basic Res Cardiol. 1986;81:39–50.
16. Suga H, Hisano R, Goto Y, Yamada O, Igarashi Y. Effect of positive inotropic agents on the relation between oxygen consumption and systolic pressure volume area in canine left ventricle. Circ Res. 1983;53:306–18.
17. Topilsky Y, Oh JK, Atchison FW, Shah DK, Bichara VM, Schirger JA, Kushwaha SS, Pereira NL, Park SJ. Echocardiographic findings in stable outpatients with properly functioning HeartMate II left ventricular assist devices. J Am Soc Echocardiogr. 2011;24:157–69.
18. Maybaum S, Mancini D, Xydas S, Starling RC, Aaronson K, Pagani FD, Miller LW, Margulies K, McRee S, Frazier OH, Torre-Amione G, LVAD Working Group. Cardiac improvement during mechanical circulatory support: a prospective multicenter study of the LVAD Working Group. Circulation. 2007;115:2497–505.
19. McConnell PI, Del Rio CL, Kwiatkowski P, Farrar DJ, Sun BC. Assessment of cardiac function during axial-flow left ventricular assist device support using a left ventricular pressure-derived relationship: comparison with pre-load recruitable stroke work. J Heart Lung Transplant. 2007;26:159–66.
20. Drakos SG, Kfoury AG, Selzman CH, Verma DR, Nanas JN, Li DY, Stehlik J. Left ventricular assist device unloading effects on myocardial structure and function: current status of the field and call for action. Curr Opin Cardiol. 2011;26:245–55.

J Artif Organs (2012) 15:140–145
DOI 10.1007/s10047-011-0613-5

ORIGINAL ARTICLE

Effect of the technique for assisting renal blood circulation on ischemic kidney in acute cardiorenal syndrome

Shigeru Hanada · Yoshiaki Takewa · Toshihide Mizuno · Tomonori Tsukiya · Yoshiyuki Taenaka · Eisuke Tatsumi

Received: 3 February 2011 / Accepted: 10 October 2011 / Published online: 21 October 2011

Abstract The technique for assisting renal blood circulation may be a useful therapeutic method in acute cardiorenal syndrome (ACRS), because renal ischemic dysfunction due to the reduced renal blood circulation is a powerful negative prognostic factor in ACRS. We constructed a circuit assisting renal arterial pressure and flow, and performed renal-selective blood perfusion (RSP) to the left kidney in a goat model of ACRS induced by right ventricular rapid pacing ($n = 8$), with the right kidney left intact as an internal control. Upon induction of ACRS, renal arterial flow (RAF), creatinine clearance (CCr), and renal oxygen consumption (RVO_2) of the left kidney decreased to 49, 48, and 63% of the respective baseline values accompanied by a significant increase in renal vascular resistance (RVR), and similar results were observed in the right kidney. Then, RSP improved RVR and increased left RAF, CCr, and RVO_2 up to 91, 86, and 93% of baseline values, respectively, without a significant change in systemic hemodynamics. The RSP-treated kidney showed significantly higher CCr and urinary excretion of water and sodium compared to the contralateral kidney. Additional infusion of prostaglandin E_1 with RSP decreased RVR further and enabled the left RAF to increase up to 129% of the baseline value, without a significant change in systemic hemodynamic parameters. The CCr and RVO_2 did not change significantly, and urinary excretion of water and sodium showed a tendency to increase. These findings suggest that the technique for assisting renal blood circulation for both kidneys may offer a new treatment strategy for patients with ACRS.

Keywords Cardiorenal syndrome · Extracorporeal circulation · Renal blood flow · Renal-selective blood perfusion

S. Hanada (✉) · Y. Takewa · T. Mizuno · T. Tsukiya · Y. Taenaka · E. Tatsumi
Department of Artificial Organs, Research Institute, National Cerebral and Cardiovascular Center, 5-7-1 Fujishiro-dai, Suita, Osaka 565-8565, Japan
e-mail: s-hanada@umin.ac.jp

Introduction

New medical devices [1–3] assisting systemic blood circulation with innovative methods have appeared in recent years. We are planning to develop a new technique that enables assisting the blood circulation of a specific organ selectively with a compact device. Above all, the technique for assisting the renal blood circulation may be a useful therapeutic method, because renal ischemia is a well-known common cause of renal dysfunction, especially in the condition of acute cardiorenal syndrome (ACRS) [4]. ACRS is a condition in which acute heart dysfunction leads to development of acute renal dysfunction, with each accelerating the progression of the other. ACRS is commonly heralded by the appearance of progressive worsening of renal function and retention of sodium and water accompanied by diuretic resistance [4–6], and the worsening of renal function is a powerful independent prognostic factor for adverse outcomes [7, 8]. However, the effective treatment strategy for renal hypoperfusion has not been developed yet. Then we hypothesized that optimizing renal hemodynamics by perfusion of blood flow into the renal artery selectively could be effective for preserving renal function and promoting diuresis with little influence on the systemic circulation. In this study, we constructed an extracorporeal circuit for perfusing the blood with normal arterial pressure to a kidney and evaluated the effects on renal outcome in a goat model of ACRS.

Materials and methods

Animals and experimental procedure

Adult goats [$n = 8$, mean (±SD) weight 53.0 ± 5.6 kg] were used in the study. The animals were cared for by well-trained staff, including veterinarians, in accordance with the Principles of Laboratory Animal Care and Use of Laboratory Animals of the National Academy of Sciences, as published by the US National Institutes of Health (NIH).

Under general anesthesia with isoflurane and muscle relaxation with suxamethonium chloride, volume-controlled ventilation (Servo 900C, Siemens Elema AB, Sweden) was performed to maintain an arterial carbon dioxide pressure ($PaCO_2$) of 35–45 mmHg and an arterial oxygen pressure (PaO_2) of 100–200 mmHg. Isotonic saline was infused at a rate of 100 ml/h from 2 days before to the end of the experiment to produce sufficient urine flow to give reliable measurements of creatinine clearance (CCr). Infusion of an initial bolus of heparin 2,000 IU followed by continuous infusion at 20 IU/kg/h was performed to prevent blood coagulation. A pulmonary artery thermodilution catheter (CCO Pulmonary Artery Catheter, Edwards Lifesciences LLC, Irvine, CA, USA) was inserted from the left jugular vein and guided into the pulmonary artery for continuous measurement of cardiac output (CO). A bipolar temporary pacing catheter (CI-500C, Harmac Medical Products, Inc., Buffalo, NY, USA) was inserted from the left jugular vein and guided into the right ventricle. Catheters were inserted into the left carotid artery and superior vena cava to monitor the aortic pressure (AoP) and central venous pressure (CVP), respectively.

The abdomen was opened through a midline incision, and the left renal artery and vein were exposed. An electromagnetic flow probe (MVF-2100, Nihon-Kohden, Japan) was placed around the left renal artery for monitoring the renal arterial blood flow (RAF) of the left kidney. The left renal vein was cannulated with a catheter to monitor the renal venous pressure (RVP). Catheters (All Silicone Foley Balloon Catheter 2-way pediatric 6-Fr 1-ml Transparent type, Create Medic, Japan) were inserted into both ureters from the ureteral openings in the bladder retrogradely for urine collection from each kidney. The right kidney was left intact for use as an internal control. This condition was defined as the baseline state.

Right ventricular rapid pacing at 200–230 beats/min was then performed to produce CO <60% of baseline, mean AoP <65 mmHg, and left RAF <60% of baseline. This condition was defined as the ACRS state. After attainment of this state, the pacing rate was controlled to maintain a mean AoP of 55–65 mmHg for the remainder of the study.

The circuit is composed of a roller pump, uptake and return cannulas, and connecting tubing. The blood capacity was approximately 120 ml and was primed with saline. The uptake cannula [Capiox EBS Cannula Kit (Venous Kit, 18-Fr Catheter), Terumo Corp., Japan] was inserted into the right carotid artery with the tip positioned at the aorta. The return cannula (a Gundry 10-Fr polyethylene catheter; Medtronic Inc., Cary, NC, USA) was inserted into the left renal artery surgically within a few minutes after measurements in the ACRS state. Then the pump was activated and the blood flow rate (adjusted in minimal steps of 10 ml/min) was controlled to maintain the renal arterial pressure (RAP) of the left kidney at 80–85 mmHg, which was the baseline level of the mean AoP. All the RAF of the left kidney was supplied by the circuit without native blood flow, because the renal artery was occluded with a balloon of the catheter. We named the technique renal-selective blood perfusion (RSP) and defined this condition as the RSP state. Furthermore, we infused the prostaglandin E_1 (PGE_1) drug, alprostadil alfadex, into the RSP-treated renal artery selectively from the side arm of the circuit at a rate of 0.015 μg/kg/min and defined this condition as the RSP + PGE_1 state.

Urine was collected for 60 min after approximately 10 min of equilibration to stabilize the hemodynamics in each condition, and three blood samples each were collected from the aorta, central vein, left renal artery (only for RSP and RSP + PGE_1), and left renal vein at the end of each condition. Mean values from these samples were used in the analysis. Pressors and diuretics were not used throughout the study.

Measurement of parameters

Urine outcomes for each kidney were assessed in terms of urine flow rate (UF), the amount of urinary sodium excretion (UNa), and CCr using data for creatinine and sodium ion levels in arterial blood and urine samples. UNa and CCr were calculated as follows: UNa (μEq/min) = urinary sodium concentration (μEq/ml) × UF (ml/min); CCr (ml/min) = urine creatinine level (mg/dl) × UF (ml/min)/serum creatinine level (mg/dl).

Mean systemic vascular resistance (SVR) and renal vascular resistance (RVR), which represent the total resistance in the kidneys, were calculated as follows: SVR (dyne s cm^{-5}) = (AoP − CVP) (mmHg)/CO (l/min) × 79.92; RVR (dyne s cm^{-5}) = (RAP − RVP) (mmHg)/RAF (ml/min) × 1,000 × 79.92.

Oxygen metabolism in the RSP-treated kidney was assessed in terms of oxygen delivery (RDO_2) and oxygen consumption (RVO_2), using data from blood gas analysis (ABL 800, Radiometer, Copenhagen, Denmark). These parameters were calculated as follows: RDO_2 (ml O_2/min) = RAF × $rCaO_2$

and RVO_2 (ml O_2/min) = RAF × ($rCaO_2$ − $rCvO_2$), where $rCaO_2$ and $rCvO_2$ represent the renal arterial and venous oxygen contents, respectively: $rCaO_2$ (ml/dl) = serum hemoglobin level (Hb, mg/dl) × 1.34 × renal arterial oxygen saturation (%) + 0.003 × renal arterial oxygen pressure (mmHg); $rCvO_2$ (ml/dl) = Hb × 1.34 × renal venous oxygen saturation (%) + 0.003 × renal venous oxygen pressure (mmHg).

Statistical analysis

Data are expressed as mean ± SD. Differences in parameters between two groups under the same conditions were evaluated by Student's t test. Differences in parameters among four conditions were evaluated by two-way ANOVA, followed by a Dunnett's post hoc test. $P < 0.05$ was considered significant. All analyses were performed using SPSS for Windows, v.16 (SPSS Inc., Chicago, IL, USA).

Results

In ACRS condition, the mean CO dropped to 47% ($P < 0.001$) of the baseline level, and SVR increased significantly (Fig. 1). The mean RAF of the left kidney dropped to 49% ($P < 0.001$), accompanied by a significant increase in RVR ($P = 0.003$), which was calculated by substituting the mean AoP for RAP before initiation of RSP (Fig. 2). UF, UNa, and CCr in the left kidney decreased to 34% ($P < 0.001$), 38% ($P < 0.001$), and 48% ($P < 0.001$) of the respective baseline values, and similar results were observed in the right kidney (Fig. 3). RDO_2 and RVO_2 of the left kidney also decreased to 48% ($P < 0.001$) and 63% ($P < 0.001$) of the respective baseline values (Fig. 2).

When starting RSP, the initial RSP flow rate was insufficient because of the increased RVR. However, RSP decreased RVR gradually, which enabled an increase in flow rate. As the flow rate increased, RVR showed a rapid but transient increase and then decreased gradually, allowing the flow rate to increase further. Thus, careful flow control was needed, and about 10–15 min was required to reach a stable RSP flow at the targeted perfusion pressure. After establishing equilibration for this condition, RAF of the RSP-treated left kidney reached 91% of baseline ($P = 0.294$) and 184% of the ACRS level ($P < 0.001$). This was accompanied by a significant improvement in RVR compared to the ACRS level ($P = 0.021$) with reestablishment of the baseline level ($P = 0.449$) without a significant change in systemic hemodynamic parameters (Figs. 1, 2). CCr of the RSP-treated kidney significantly improved up to 86% of baseline ($P = 0.728$), and it was significantly higher than the 43% of baseline clearance for the non-perfused contralateral kidney in the same condition ($P < 0.001$). UF and UNa also increased significantly (both $P < 0.001$ vs. ACRS levels), and they were higher than the values for the contralateral kidney, which both showed marked decreases (both $P < 0.001$) (Fig. 3). UNa was significantly higher ($P < 0.001$), and UF showed a tendency to be higher ($P = 0.056$) than the baseline levels of the same kidney (Fig. 3). RDO_2 and RVO_2 improved significantly (both $P < 0.001$ vs. ACRS levels) and reached 91% and 93% of the respective baseline levels ($P = 0.277$ and 0.148, respectively) (Fig. 2).

RSP + PGE_1 decreased RVR significantly ($P = 0.021$) and increased RAF to 129% of the level with RSP alone ($P = 0.047$) (118% of the baseline level, $P = 0.557$) without a significant change in SVR ($P = 0.432$) (Figs. 1, 2). CCr for the RSP + PGE_1-treated kidney was 96% of the clearance with RSP alone, with no significant change ($P = 0.634$). UF and UNa showed a tendency to increase and reached 123 and 115% of the respective values with RSP alone ($P = 0.192$ and $P = 0.280$, respectively). In contrast, there was a tendency for lower values for the non-perfused contralateral kidney (Fig. 3). RDO_2 increased significantly to 126% of the value with RSP alone ($P = 0.047$), and RVO_2 showed little change ($P = 0.492$) (Fig. 2). After the study, the urine flow disappeared within minutes after the pump was stopped.

Discussion

The important causes for development of renal dysfunction in ACRS are supposed to be the reduced renal arterial pressure and flow caused by the worsened CO. The reduced renal arterial pressure and flow lead to neurohumoral activations including the renin-angiotensin system, sympathoadrenal system, and arginine-vasopressin system. These factors lead to excess peripheral and intrarenal vasoconstriction, further decreasing the renal blood flow and glomerular filtration rate (GFR) and leading to a decrease in renal function, causing damage that is initially reversible but ultimately irreversible [4–6]. This study showed that the improvement of renal arterial pressure and flow by RSP can improve RVR and glomerular function, and facilitate the production of urinary excretion of sodium and water in a goat model of ACRS. The improvement of the renal oxygen consumption, which reflects the change of GFR [9, 10], supported the findings. These findings may indicate that this technique has the possibility to reverse signals for intrarenal vasoconstriction and may break the vicious cycle of ACRS described above.

Recently, compact and less invasive mechanical circulatory devices have been developed [1–3]. A percutaneous

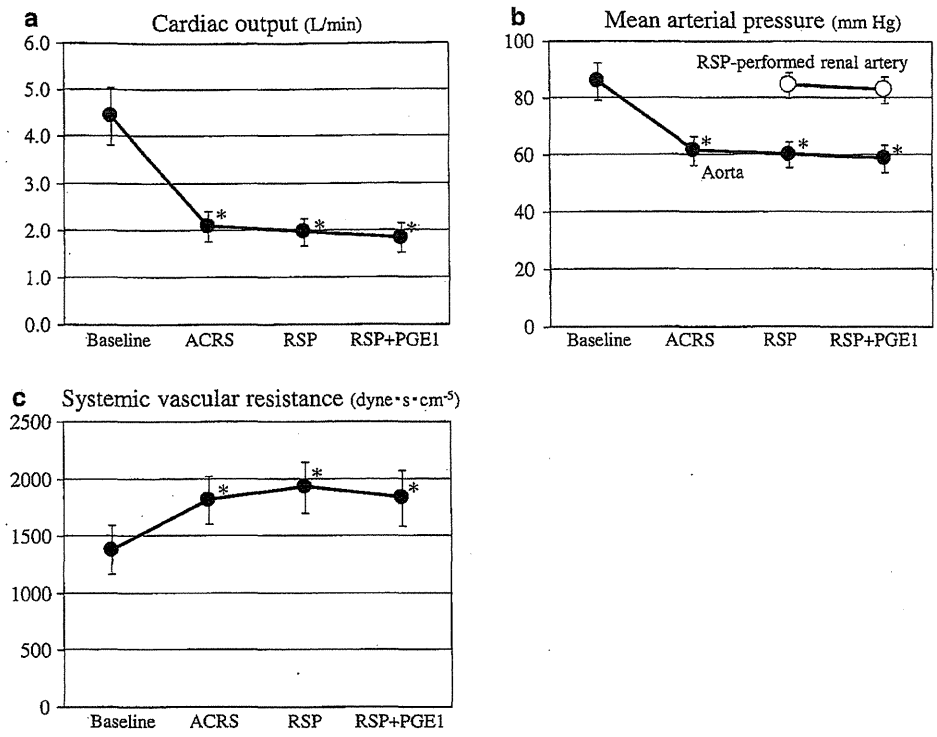

Fig. 1 **a** Cardiac output, **b** mean systemic aortic pressure (*black circles*), and renal arterial pressure in the renal-selective arterial blood perfusion (RSP)-treated kidney (*white circles*), and **c** systemic vascular resistance at baseline and under ACRS, RSP, and RSP + PGE_1 conditions in a goat model of acute cardiorenal syndrome ($n = 8$). $^*P < 0.05$ versus baseline

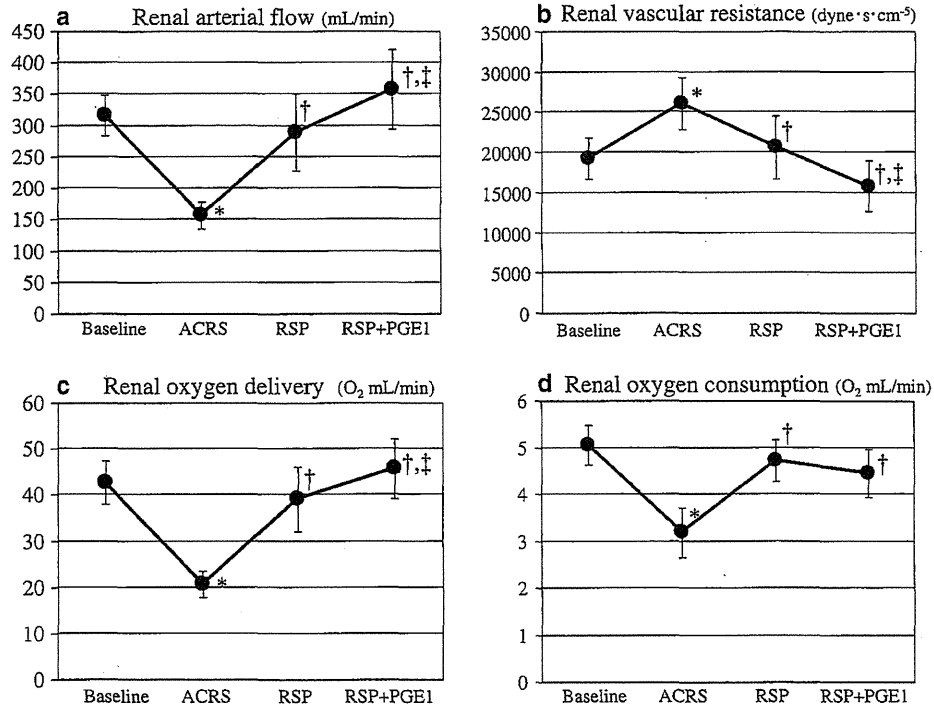

Fig. 2 **a** Renal arterial flow, **b** renal vascular resistance, **c** renal oxygen delivery, and **d** renal oxygen consumption in the renal-selective arterial blood perfusion (RSP)-treated the kidney at baseline and under ACRS, RSP, and RSP + PGE_1 conditions in a goat model of acute cardiorenal syndrome ($n = 8$). $^*P < 0.05$ versus baseline; $^{\dagger}P < 0.05$ versus ACRS; $^{\ddagger}P < 0.05$ versus RSP

catheter with a microaxial blood pump of external diameter less than 6 mm, as implemented in the miniaturized Impella™ cardiac support system, has been applied in practical use [1]. If an intravascular blood pump system that is so small as to be installed in the aorta is realized in the near future, a bifurcated catheter with an intravascular catheter-mounted blood pump that can perfuse blood to both kidneys percutaneously through a single access site will be realized. The approach may be able to deliver sufficient blood flow to the kidney without having a large

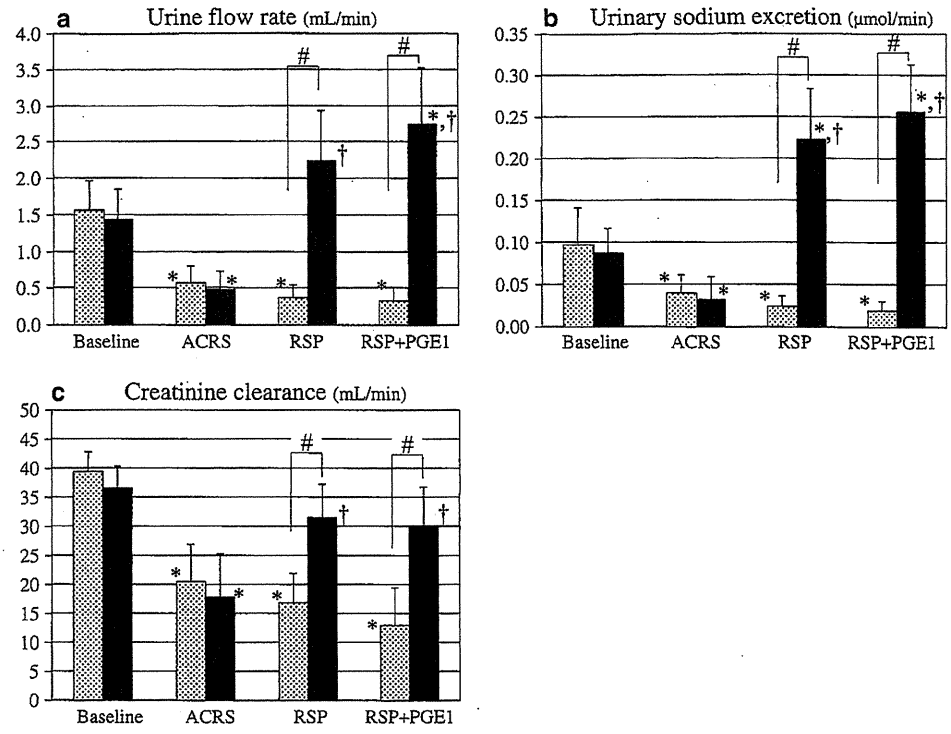

Fig. 3 **a** Urine flow rate, **b** urinary sodium excretion, and **c** creatinine clearance of the renal-selective arterial blood perfusion (RSP)-treated kidney (*black bars*) and control kidney (*dotted bars*) at baseline and under ACRS, RSP, and RSP + PGE_1 conditions in a goat model of acute cardiorenal syndrome ($n = 8$). $^*P < 0.05$ versus baseline in the same kidney; $^\dagger P < 0.05$ versus ACRS in the same kidney; $^\#P < 0.05$ versus the control kidney under the same condition

influence on the systemic circulation or systemic fluid loading, which may worsen cardiac congestion.

Patients with ACRS often fail to achieve adequate diuresis with high-dose diuretics and require mechanical fluid removal via methods such as ultrafiltration. However, ultrafiltration, which controls systemic fluid loading, often fails to preserve renal function clinically. It remains unclear whether diuretics [11, 12] or ultrafiltration [13] prevent worsening of renal function or improve the outcome. In contrast, this method improves the renal arterial pressure and flow directly, and is effective for preserving renal function, as indicated in this study. The preserved renal function may be favorable for cardiac unloading, which may break the vicious cycle of ACRS and may lead to the improved prognosis of the disease. Thus, this method is a possible alternative to high dose diuretics or hemofiltration therapy.

The technique in the present study enables infusing therapeutic agents to the kidney selectively. Delivery of therapeutic agents directly to the kidneys has the advantage of providing a higher local effective dose with potentially greater renal effects, while limiting systemic exposure and adverse effects because of renal first-pass elimination. The rationale for using PGE_1 included its properties as a potent vasodilator and its reported benefit in preventing renal ischemia under hypoperfusion and ischemia [14, 15]. The rate of 0.015 μg/kg/min of PGE_1 for a kidney was arbitrarily determined based on data showing that low systemic infusion rates of PGE_1 below 0.032 μg/kg/min do not cause a change in blood pressure or heart rate in healthy humans [16, 17]. The renal-selective infusion of PGE_1 with RSP exerted vasodilating effects on the renal vascular system without having a significant effect on the systemic vascular system, which enabled an increase in the RSP flow and resulted in increased oxygen delivery, which should be favorable for treatment of ACRS. The findings that PGE_1 tended to increase water and sodium excretion are supported by several studies showing diuretic and natriuretic effects of PGE_1 [18, 19]. These findings indicate beneficial effects of additional infusion of PGE_1 when performing RSP.

The experimental procedure used in the study has a few limitations. First, this study was performed under the condition of anesthesia. Second, this study was limited to a short-term evaluation, while clinical treatment of ACRS usually takes days or even weeks, and the efficacy of RSP for a kidney with long-term hypoperfusion is unknown. The short evaluation time may have prevented clarification of the effects of promotion of diuresis on the systemic circulation. Third, the evaluation of renal function using CCr has limitations. The CCr tends to be higher than GFR in a kidney with markedly decreased function because the small amount of creatinine secreted from renal tubules to urine has a significant influence on the calculation of CCr in such a kidney. Finally, the presence of the contralateral kidney, which was perfused at systemic arterial pressure as a control, could have been a confounding factor. The major confounding effect would have been the difference in

neurohumoral activities between kidneys, which prevented neurohumoral evaluation. Further studies of the effects of RSP on both kidneys over a few days are needed to address these issues.

In conclusion, this study showed that the technique for assisting renal blood circulation improved RVR and glomerular function, and facilitated the production of urinary excretion of sodium and water in a goat model of ACRS. This technique for both kidneys may have the possibility to be a new treatment strategy for patients with ACRS. We believe that the development of techniques for assisting blood circulation of a specific organ selectively with a compact device will be a new theme in the field of study of artificial organs.

References

1. Meyns B, Stolinski J, Leunens V, Verbeken E, Flameng W. Left ventricular support by catheter-mounted axial flow pump reduces infarct size. J Am Coll Cardiol. 2003;41:1087–95.
2. Reitan O, Steen S, Ohlin H. Hemodynamic effects of a new percutaneous circulatory support device in a left ventricular failure model. ASAIO J. 2003;49:731–6.
3. Konstam MA, Czerska B, Böhm M, Oren RM, Sadowski J, Khanal S, Abraham WT, Wasler A, Dahm JB, Gavazzi A, Gradinac S, Legrand V, Mohacsi P, Poelzl G, Radovancevic B, Van Bakel AB, Zile MR, Cabuay B, Bartus K, Jansen P. Continuous aortic flow augmentation: a pilot study of hemodynamic and renal responses to a novel percutaneous intervention in decompensated heart failure. Circulation. 2005;112:3107–14.
4. Ronco C, Haapio M, House AA, Anavekar N, Bellomo R. Cardiorenal syndrome. J Am Coll Cardiol. 2008;52:1527–39.
5. Rea ME, Dunlap ME. Renal hemodynamics in heart failure: implications for treatment. Curr Opin Nephrol Hypertens. 2008;17:87–92.
6. Anand IS, Chugh SS. Mechanisms and management of renal dysfunction in heart failure. Curr Opin Cardiol. 1997;12:251–8.
7. Metra M, Nodari S, Parrinello G, Bordonali T, Bugatti S, Danesi R, Fontanella B, Lombardi C, Milani P, Verzura G, Cotter G, Dittrich H, Massie BM, Dei Cas L. Worsening renal function in patients hospitalised for acute heart failure: clinical implications and prognostic significance. Eur J Heart Fail. 2008;10:188–95.
8. de Silva R, Nikitin NP, Witte KK, Rigby AS, Goode K, Bhandari S, Clark AL, Cleland JG. Incidence of renal dysfunction over 6 months in patients with chronic heart failure due to left ventricular systolic dysfunction: contributing factors and relationship to prognosis. Eur Heart J. 2006;27:569–81.
9. Kiil F, Aukland K, Refsum HE. Renal sodium transport and oxygen consumption. Am J Physiol. 1961;201:511–6.
10. Kurnik BR, Weisberg LS, Kurnik PB. Renal and systemic oxygen consumption in patients with normal and abnormal renal function. J Am Soc Nephrol. 1992;2:1617–26.
11. Mehta RL, Pascual MT, Soroko S, Chertow GM, PICARD Study Group. Diuretics, mortality, and nonrecovery of renal function in acute renal failure. JAMA. 2002;288:2547–53.
12. The SOLVD Investigators. Effect of enalapril on survival in patients with reduced left ventricular ejection fractions and congestive heart failure. N Engl J Med. 1991;325:293–302.
13. Costanzo MR, Guglin ME, Saltzberg MT, Jessup ML, Bart BA, Teerlink JR, Jaski BE, Fang JC, Feller ED, Haas GJ, Anderson AS, Schollmeyer MP, Sobotka PA, UNLOAD Trial Investigators. Ultrafiltration versus intravenous diuretics for patients hospitalized for acute decompensated heart failure. J Am Coll Cardiol. 2007;49:675–83.
14. Arbid EJ, Hakaim AG, LaMorte WW, Menzoian JO. Prevention of renal cortical ischemia during aortic clamping with prostaglandin E1. Arch Surg. 1995;130:326–30 (discussion 330–1).
15. Mahmoud IM, Hussein Ael-A, Sarhan ME, Awad AA, El Desoky I. Role of combined L-arginine and prostaglandin E1 in renal ischemia-reperfusion injury. Nephron Physiol. 2007;105:57–65.
16. Wilkens JH, Wilkens H, Elger B, et al. Cardiac and microcirculatory effects of different doses of prostaglandin E1 in man. Eur J Clin Pharmacol. 1987;33:133–7.
17. Brecht T, Ayaz M. Circulation parameters during intravenous and intra-arterial administration of increasing doses of prostaglandin E1 in healthy subjects. Klin Wochenschr. 1985;63:1201–4.
18. Lum GM, Aisenbrey GA, Dunn MJ, Berl T, Schrier RW, McDonald KM. In vivo effect of indomethacin to potentiate the renal medullary cyclic AMP response to vasopressin. J Clin Invest. 1977;59:8–13.
19. Grantham JJ, Orloff J. Effect of prostaglandin E1 on the permeability response of the isolated collecting tubule to vasopressin, adenosine 3′,5′-monophosphate, and theophylline. J Clin Invest. 1968;47:1154–61.

Regular Paper

Miniaturized Axial Gap Maglev Motor with Vector Control for Pediatric Artificial Heart

Masahiro OSA[*1] (Stu. Mem.), Toru MASUZAWA[*1] (Mem.) and Eisuke TATSUMI[*2]

We have developed a maglev ventricular assist device (VAD) for use in infant patients, which requires the device size to be smaller compared to adult devices. Moreover, the rotor speed of the pediatric VAD must be varied over a wide range of 2000 to 5000 rpm according to the hemodynamics of the growing pediatric patients. In this research, a miniaturized axial gap type double stator maglev motor is reported. The double stator maglev motor consists of a top stator, a bottom stator and a levitated rotor set between the stators which have an identical structure. A double stator mechanism has been adopted to enhance a motor torque with smaller device size and a large air-gap. The rotating speed and the axial position of the rotor are regulated independently based on a vector control algorithm which can generate an axial attractive force and a torque with a single rotating magnetic field. The diameter and a height of the developed motor are 24 mm and 43 mm, respectively. The developed motor can produce an axial force and a torque independently by using vector control, and also succeeded in levitation and rotation up to a rotational speed of 3000 rpm. The developed motor indicates a potential for the pediatric VAD.

Keywords: maglev motor, double stator mechanism, vector control algorithm, pediatric ventricular assist device.
(*Received: 7 October 2011, Revised: 15 February 2012, 8 May 2012, 18 May 2012, Accepted: 22 May 2012*)

1. Introduction

Pediatric ventricular assist devices (VADs) require the device to be smaller in size and have better durability compared to adult devices. In addition, it is necessary to regulate the blood flow rate by varying the rotational speed of the rotor over a wide operational range from 2000 rpm to 5000 rpm. Active magnetic bearings, which can eliminate mechanical contacting components such as contact bearings and seals from the device, offers longer device lifetime and better blood compatibility of the blood pump [1]. Several axial double stator self-bearing motors, such as a combination of a permanent magnets and a reluctance motors [2] or double permanent motors [3-4], were developed. Self-bearing motors for use in paediatric VADs are required to be miniaturized, and have large air-gap, i.e., more than 1.5 mm, in order to avoid the blood damage due to high shear stress. The reluctance motor which does not have permanent magnets has disadvantage in terms of producing the sufficient magnetic suspension forces and rotating torque with a smaller device size and large air-gap. The double permanent motors require another passive or active magnetic bearing to support the radial direction or inclination of the rotor. We have developed a miniaturized 3-degrees of freedom (3-DOF) control axial gap type double stator maglev permanent magnet motor for use in paediatric VAD, which had adopted a vector control algorithm. The developed double permanent motor can be miniaturized and have large air-gap because the permanent magnet produce the higher magnetic flux density in the air-gap. Furthermore the developed motor can actively control 3-DOF of the rotor without an additional passive or active magnetic bearing. In this paper, the double stator maglev motor is presented and feasibility of levitated rotation with the vector control is evaluated.

Correspondence: T. MASUZAWA, Department of Mechanical Engineering, Ibaraki University, 4-12-1 Nakanarusawa, Hitachi, Ibaraki 316-8511, Japan
email: masuzawa@mx.ibaraki.ac.jp
[*1] Ibaraki University

2. Structure and Principle of Double Stator Motor

2.1 Structure of Double Stator Maglev Motor

Fig.1 shows a schematic of double stator maglev motor. The self-bearing motor consists of a top stator, a bottom stator and a levitated rotor set between the stators. Both stators have an identical structure. The rotor is suspended axially. We have developed a double stator mechanism to enhance motor torque with a smaller device size and large air-gap. The top and bottom stators have six slots, and two coils of bottom stators have six slots, and two types of concentrated winding coils are set on each teeth. One of these windings is to control the axial position and rotating speed of the rotor. The other coil is to control the inclination of the rotor. The rotor includes two poles permanent

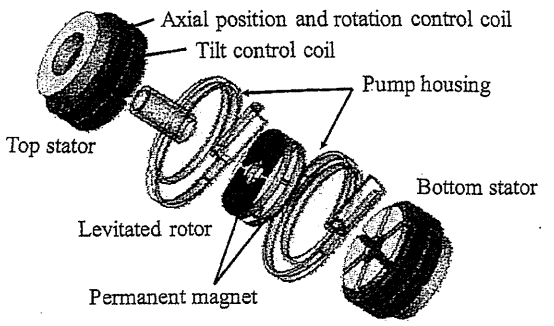

Fig. 1. Basic structure of double stator maglev motor.

magnets on the both its surfaces faced the top and the bottom stators. The axial position and the rotating speed of the rotor are regulated independently using a vector control based algorithm which can generate an axial attractive force and rotating a torque with a single rotating magnetic field. The radial position of the rotor is restricted by passive stability.

2.2 Principle of Vector Control Algorithm

Fig. 2 shows the schematic of the vector control algorithm with double stator mechanism. Three-phase currents are fed into the motor coils to produce an attractive force and a rotating torque. The axial force and the rotating torque will be regulated by changing the magnitude and the phase difference of the magnetic flux based on the vector control algorithm [5]. The stator electromagnet and the permanent magnets of the rotor are assumed to produce the sinusoidal rotating magnetic fields which have peak flux density of B_e and B_p respectively. And these magnetic fields have phase difference of ψ. These flux in the air-gap are generated in the axial direction, i.e. z-axis direction, and has constant values independently of the radial coordinate r.

$$B_E(\theta_Z,t) = B_e\cos(\omega t - \theta_Z) \tag{1}$$

$$B_P(\theta_Z,t) = B_p\cos(\omega t - \theta_Z - \psi) \tag{2}$$

Where θ_Z is angler coordinate around z-axis and ω is rotating speed of the rotor. An axes of coordinate is displayed in Fig. 2. A demagnetization curve of the permanent magnet is assumed to have linear characteristic, and load line of the permanent magnet has linear relationship for flux density B_p in terms of coercivity of H_p.

$$B_p = \frac{B_r}{H_{cb}}H_p + B_r \tag{3}$$

$$B_p = \mu_0\frac{l}{z}H_p \tag{4}$$

From these equations, the peak value of the flux density produced by the rotor permanent magnet can be calculated as follow.

$$B_p = \left(\frac{1}{B_r} + \frac{z}{l}\cdot\frac{1}{\mu_0 H_{cb}}\right)^{-1} \tag{5}$$

Where the mean core length and the air-gap length between the rotor and the stator are defined as l and z. μ_0 is the permeability of the air-gap which is assumed to be same with it of the vacuum. The remanent flux density and the coercivity of the permanent magnet are described as B_r and H_{cb}.

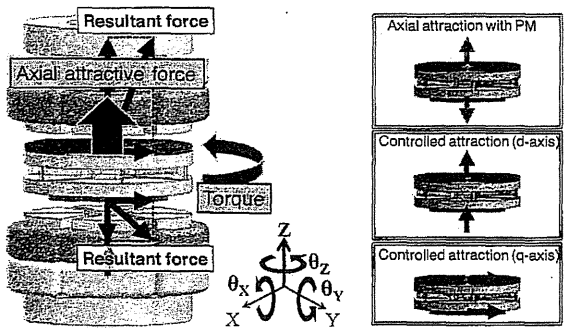

Fig. 2. Principle of vector control.

For simplicity, magnetic properties inside the rotor and the stator are assumed to be homogenous and the reluctance of the core is ignored when compared with that of the air-gap. The peak value of the flux density produced by the electromagnet can be shown in terms of turn number of windings which defined as N and peak excitation current I_e to produce the flux density B_e.

$$B_e = \frac{\mu_0 N I_e}{z} \tag{6}$$

The magnetic stored energy, which is defined as W_g, can be expressed in terms of the energy density of the magnetic flux density integrated over the volume in the air-gap of the motor. Then the axial force F_z and rotating torque τ_z produced by a single stator can be expressed as follows [6-8],

$$F_z = \frac{\partial W_g}{\partial z} = \frac{(r_2^2 - r_1^2)\pi}{4\mu_0}\{B_p^2 + 2B_pB_e\cos\psi + B_e^2\} \tag{7}$$

$$\tau_z = \frac{\partial W_g}{\partial \psi} = \frac{zM(r_2^2 - r_1^2)\pi}{2\mu_0}B_pB_e\sin\psi \tag{8}$$

Where r_1 and r_2 are the inner and outer radii of the rotor. To control the axial position and the torque of the rotor independently, the stator flux density B_e is divided into the direct axis component B_d and the quadrature axis component B_q corresponding to the flux components in the direction of the permanent magnet. B_d and B_q are defined as follows,

$$B_d = \sqrt{\tfrac{3}{2}}B_e\cos\psi = \sqrt{\tfrac{3}{2}}\frac{\mu_0 N I_e}{z}\cos\psi \tag{9}$$

$$B_q = \sqrt{\tfrac{3}{2}}B_e\sin\psi = \sqrt{\tfrac{3}{2}}\frac{\mu_0 N I_e}{z}\sin\psi \tag{10}$$

Where we assume that the magnetic flux of the d-axis produced by the top stator and bottom stator are B_{d1} and B_{d2}, and the magnetic flux of the q-axis produced by the top stator and bottom stator are B_{q1} and B_{q2}. The magnetic flux are given as follow relationship to produce the axial attractive force and the rotating torque independently.

$$B_{d1} = -B_{d2} = B_d \tag{11}$$

$$B_{q1} = B_{q2} = B_q \tag{12}$$

A resultant attractive force is produced as a differential of the attractive force between the top stator and the bottom stator. The rotating torque is produced as summation of the rotating torque between the top stator and the bottom stator [9-11].

$$F = \sqrt{\frac{2}{3}}\frac{(r_2^2 - r_1^2)\pi}{\mu_0}B_pB_d \tag{13}$$

$$\tau = \sqrt{\frac{2}{3}}\frac{z(r_2^2 - r_1^2)\pi}{\mu_0}B_pB_q \tag{14}$$

From these equations, the motor and the attractive force is controlled with d-axis current the rotating torque is controlled with q-axis current independently.

2.3 Principle of Tilt Control

Fig. 3 shows the principle of the tilt control. The inclination of the levitated rotor is controlled by the tilt control coils which generate a uniform magnetic flux that interacts with the stator magnetic field. The interaction between the two magnetic fields produces an unbalanced magnetic flux density between the rotor and the stator surfaces. To illustrate this principal, consider only the top stator and permanent magnets of the top side of the rotor. The permanent magnet of the rotor is assumed to produce the magnetic flux density B_p. The tilt control coils produce a uniform flux density in the axial direction distributing over the air-gap and that is defined as the magnetic flux density B_T,

$$B_T = \frac{\mu_0 N I_T}{z} \tag{15}$$

where I_T is DC excitation current to produce the magnetic flux density B_T. The unbalanced axial attractive force of the N pole permanent magnet and S pole permanent magnet are described as F_N and F_S respectively. A difference between these two attractive forces produces a restoring torque τ_T.

$$\tau_T = \frac{2L(r_2^{\,2} - r_1^{\,2})}{\mu_0} B_p B_T \tag{16}$$

From the Eq. (16), the restoring torque is proportional to the tilt control flux B_T. Moreover, the inclination around x and y axes are controlled with the top and bottom stators independently, because the permanent magnets on the both rotor surfaces are set with a phase difference of 90 degrees.

2.4 Design and Manufacturing of Maglev Motor

A target pump performance of pediatric VAD is determined a maximum flow late of 1 L/min against a head pressure of 100 mmHg [12-13]. A centrifugal blood pump has been designed based on a computational fluid dynamics simulation (CFD) analysis. From the results of the CFD study, the rotational speed of the levitated rotor should be 4000 rpm to satisfy the target pump performance. When the designed pump achieves the target pump performance, an axial thrust force on the rotor is 0.14 N and a required torque is 3.5 mNm.

Fig. 4 shows a photograph of a developed double stator maglev motor made of magnetic steel core. The turn number for the axial position and torque, and for the tilt control coils are 70 turns/pole. Two Nd-Fe-B permanent magnets are mounted on both top and bottom surfaces of the rotor. The Nd-Fe-B permanent magnets, which have a coercivity of 1019 kA/m, a residual flux density of 1.32 T and have a thickness of 0.7 mm. The total height and the diameter of the developed motor are 43 mm and 24 mm, respectively. The motor has an air-gap length of 1.5 mm to the pump casing. The rotor weight and the total weight of the developed motor are 42 g and 126 g, respectively. The size of the motor is almost same as a C cell battery.

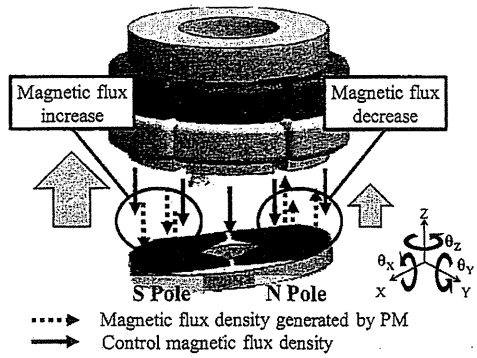

Fig. 3. Principle of tilt control.

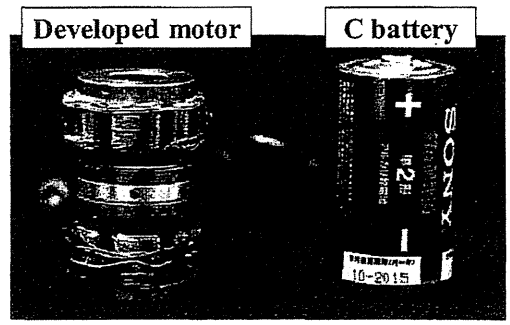

Fig. 4. Photograph of the developed motor.

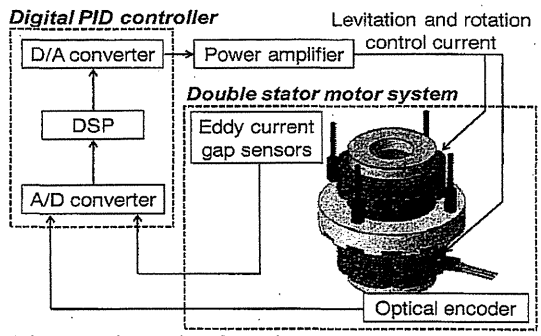

Fig. 5. Schematic of maglev motor control system.

2.5 Levitation and Rotation Control System

Fig. 5 shows the schematic of the levitation and rotation control system. Four eddy current displacement sensors are set at regular intervals to measure the axial position and tilt angles around x and y axes of the rotor. Stripe patterns are printed at circumference of the rotor to measure the rotating speed and rotating angles using an optical encoder which have a photo sensor. The rotational angles of the rotor can be detected to a sensitivity of 10 degrees. Fig. 6 and Fig. 7 show the block diagrams of the axial position, motoring control and tilt control of the rotor. Levitation and rotation controller of the motor consists of four digital PID controllers which can regulate excitation current of the electromagnets. The PID controllers of the levitation and rotation controller are implemented on a dSPACE DS1104 digital signal processor (dSPACE GmbH, Paderborn Germany) with MATLAB/Simlink.

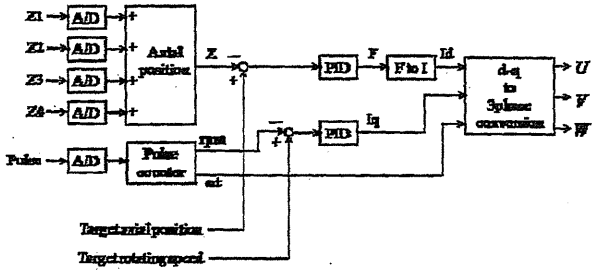

Fig. 6. Block diagram of axial position and motoring control.

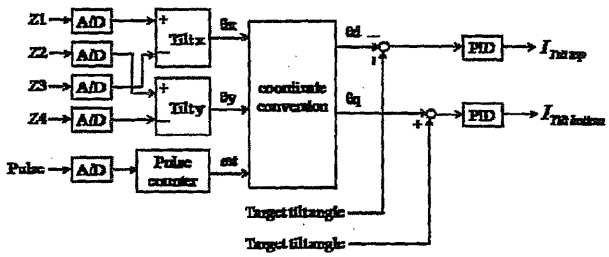

Fig. 7. Block diagram of tilt control.

3. Experiments

Fig. 8 shows an experimental setup to measure the axial force and the torque produced with the motor based on the vector control algorithm. The axial force and the torque measurement system consists of a hysteresis brake, a torque transducer, the motor stator and the rotor and a load cell. The stators are connected to the load cell and a micrometer stage, which is restricted to the axial direction. The rotor is set between both stators and is connected to the torque transducer and hysteresis brake with a shaft. The distance from the rotor surfaces to the top and bottom of the stator is 1.5 mm, respectively.

3.1 Evaluation of Static Performance

A static axial force produced by the motor was measured with fixed motor rotational direction with the hysteresis brake. The amplitude of excitation current was changed from 0 A to 2.0 A and the phase angle was varied from 0 degree to 180 degrees. The excitation current of the top stator and the bottom stator were fed to generate the magnetic flux density defined as Eqs. (9) and (13).

The static torque characteristic of the motor was measured to confirm the torque production according to the theoretical formula expressed as Eq. (14). The amplitude and the phase difference of the excitation current were varied as the same condition for the axial force measurement to vary the magnetic fields between both the stators and the rotor. The excitation current was fed into the top stator and the bottom stator based on Eqs. (10) and (12).

3.2 Evaluation of Dynamic Motor Performance

The motor dynamic torque was evaluated with varying the rotational speed from 1000 rpm to 5000 rpm.

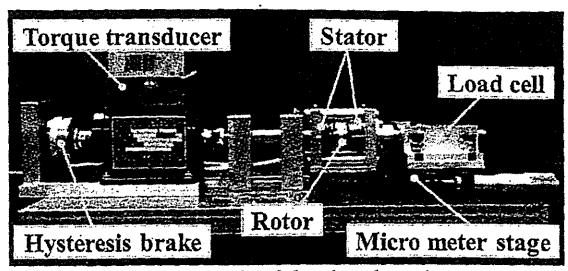

Fig. 8 Photograph of the developed motor.

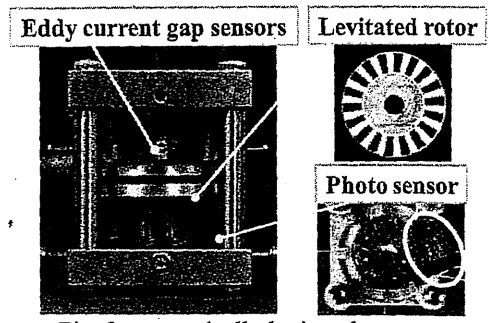

Fig. 9. magnetically levitated system.

Table 1 Control gains for PID controller.

	P Gain	Integral time	Derivertive time	Sampling interval
Axial position	25.9 [A/mm]	0.2 [sec]	0.001 [sec]	0.0001 [sec]
Rotation	0.0065 [A/rpm]	0.1 [sec]	0 [sec]	
Tilt	240 [A/rad]	1.0 [sec]	0.0035 [sec]	

The phase difference was fixed to 90 degrees at every rotational speed to check the torque production with q-axis current only. Excitation current of q-axis was regulated actively to achieve steady rotation speed with feedback control. The motor efficiency of each rotational speed was calculated from the relationship between the rotational speed, the produced torque, and the power consumption.

Independency of the axial force and the torque production with the vector control algorithm were evaluated with a fixed rotational speed of 4000 rpm which was required to achieve the target pump performance. The q-axis current was regulated depending on the load torque produced by the hysteresis brake. An axial attractive force was measured by changing d-axis current from -1 A to 1 A while the rotor was operating at this condition.

3.3 Evaluation of the Levitated Motor Performance

Fig. 9 shows a photograph of the levitation and rotation system. The developed motor was combined with the digital control system. The maximum oscillation amplitude in the axial direction and maximum tilt angles around the x and y axes of the rotor were measured to evaluate the dynamic performance of this system. The

air-gap between the both stators and the rotor was set to 1.5 mm. The movable displacement in the axial direction of the rotor was ± 0.25 mm from center position of the motor. Control gains for the PID feedback controller were determined based on limit sensitivity method. Parameters and sampling interval are shown in Table 1.

4. Results

4.1 Static Motor Performance

Fig. 10 shows a relationship between the axial attractive force and the phase difference. Solid lines show the theoretical value of axial attractive force produced by the motor which are calculated by Eqs. (5), (6) and (7). The axial attractive forces were generated as cosine wave functions according to the phase difference. The developed motor produces the axial attractive force that range from 6.6 N to -6.5 N by varying the phase difference from 0 degree to 180 degrees with an excitation current of 2.0 A. The force to excitation current gradient of the developed motor is 3.3 N/A at a phase difference of 0 degree. We define an acceleration coefficient as a mass specific force index to indicate the dynamic suspension stability against acceleration. The acceleration coefficient of the developed motor is 78.6 m/s^{2}A and indicates a sufficient performance of the magnetic suspension ability. Fig. 11 shows the relationship between the static torque and the phase difference characteristic. Solid lines show the theoretical value of static torque produced by the motor which are calculated by Eqs. (5), (6) and (8). The static torque was produced as a sine function in terms of the phase difference. The peak torque was 16.5 mNm with a phase difference of 90 degrees, and an excitation current of 2 A. The motor can generate the axial attractive force and static torque comparable in theoretical values.

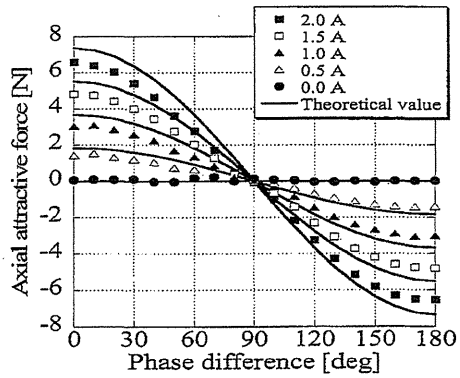

Fig. 10. The relationship between the axial attractive force and the phase difference characteristic.

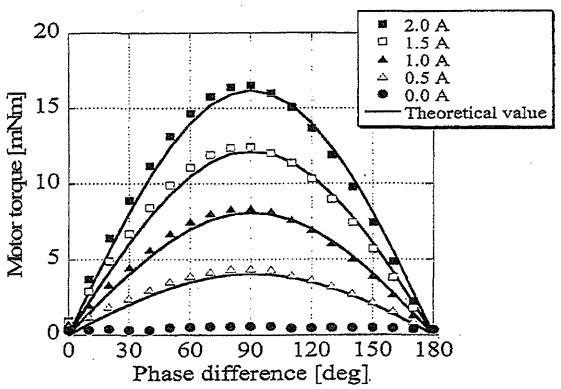

Fig. 11. The relationship between the static torque and the phase difference.

4.2 Dynamic Motor Performance

Fig. 12 shows a relationship between the power consumption and the dynamic torque. The rotor was accelerated up to 5000 rpm. The motor has a rated output power of 6.5 W at a rotational speed of 5000 rpm and a torque of 12.5 mNm. The maximum torque produced by the developed motor at a rotational speed of 4000 rpm was 14.0 mNm. A power consumption to produce a required torque of 3.5 mNm was 7.1 W. Fig.13 shows the motor efficiency with the rotating torque at each rotational speed. The motor has maximum motor efficiency of 23.1 % at a rotational speed of 4000 rpm and a torque of 6.0 mNm. At the maximum efficiency point, a power consumption of 9.4 W contains a cupper loss and a iron loss of 4.7 W and 2.5 W.

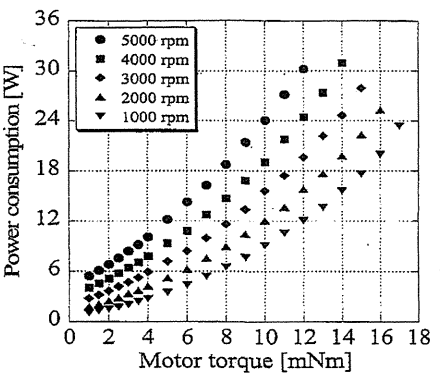

Fig. 12. Dynamic torque and power consumption characteristic.

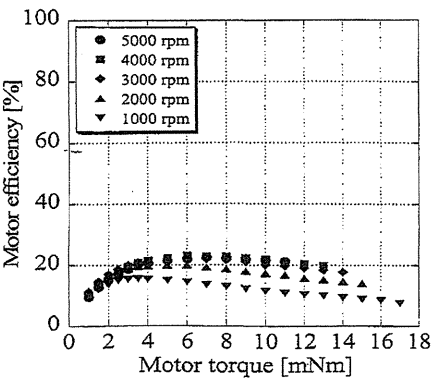

Fig. 13. Motor efficiency.

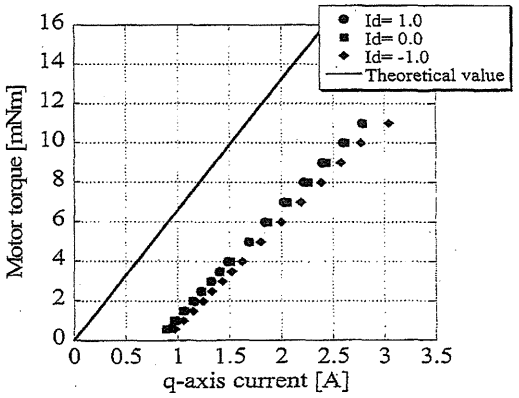

Fig. 14. Dynamic torque with q-axis current and d-axis current.

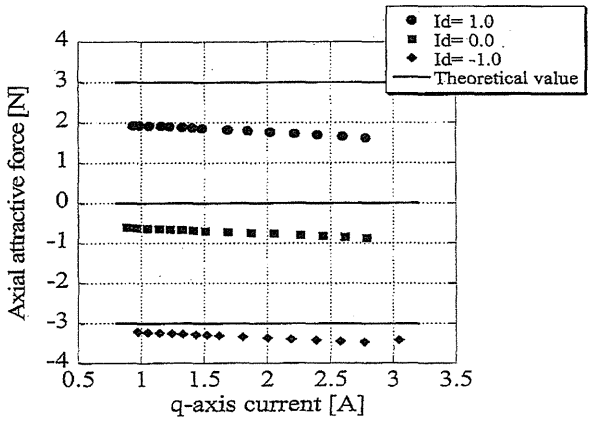

Fig. 15. Axial force with q-axis current and d-axis current.

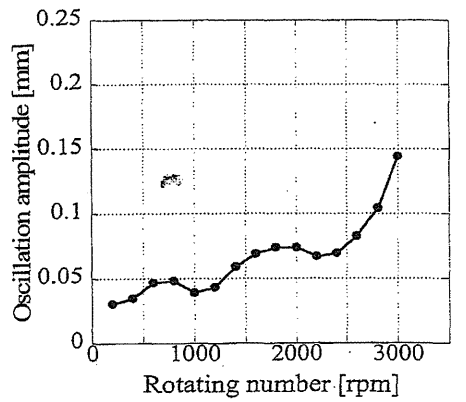

Fig. 16. Maximum oscillation amplitude in the axial direction.

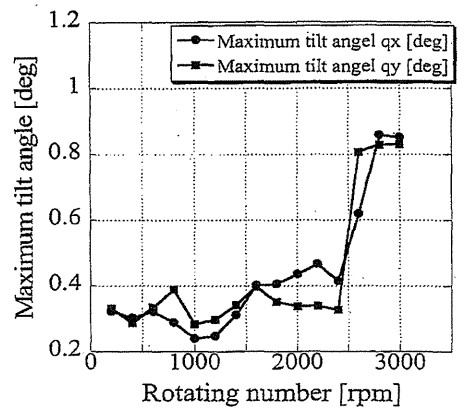

Fig. 17. Maximum tilt angles around x and y axes.

Fig.14 shows the dynamic torque produced by the q-axis current at a rotational speed of 4000 rpm. A solid line which shows the theoretical value of rotating torque against q-axis current is calculated from Eqs. (5) and (14). The torque is generated proportionally as a function of the q-axis current. The produced torque differs slightly depending on the d-axis current. The measured torque is smaller than the theoretical value. Fig.15 shows different axial attractive force produced by the d-axis current at a rotating speed of 4000 rpm. Solid lines which show the theoretical value of axial attractive force against d-axis current are calculated from Eqs. (5) and (13). The motor can vary the axial attractive force from -3 N to 2 N by changing the d-axis current in the range of ±1 A. The axial attractive force was decreased slightly with the increase of q-axis current. The measured axial attractive force has a nearly constant offset from the theoretical value at every d-axis current. The axial attractive force and the torque could be generated almost independently by using vector control algorithm, however there is a little interference each other.

4.3 Levitated motor performance

The developed motor could levitate and rotate the rotor up to 3000 rpm in the air. Fig. 16 shows a maximum axial oscillation amplitude of the rotor over each rotational speed. At rotational speeds under 2500 rpm, the vibration of the rotor was suppressed to less than 0.1 mm in the 0.25 mm clearance at each rotational speed. Fig.17 shows maximum tilt angles around the x and y axes of the rotor at each rotational speed. The tilt angles were less than 0.5 degrees in the range that the rotational speed is less than 2500 rpm.

5. Discussion

The size and power consumption of the pediatric VAD are limited to enable device implantation. The double stator structure is a strong candidate to miniaturize the maglev motor as it has higher torque production and suspension ability with a large air-gap.

From the static motor performance, the developed motor shows that it is capable of producing positive or negative attractive force and as well as unidirectional torque by changing the amplitude and the phase difference of the three-phase excitation current. The motor could vary the rotational speed of the rotor from the range of 2000 rpm to 5000 rpm which is required to change the blood flow of the pediatric VAD, and it indicate a feasibility of the developed motor for pediat-

ric ventricular assist device. However, the motor energy efficiency of 20.7 % when generating a torque of 3.5 mNm at rotational speed of 4000 rpm is little bit low. In terms of this result, we are aiming to improve the power consumption of the motor. The leakage magnetic flux must be estimated exactly in order to design a high power efficiency motor. Additionally, the material for the magnetic steel core must be chosen to reduce the iron loss caused by the higher speed rotation of the rotor in the future study.

The vector control algorithm could be adopted to the double stator proposed for this device. The vector control method should theoretically allow the axial attractive force and the torque to be regulated independently. However, the axial attractive force and torque interfered each other a little as shown in Fig. 14 and Fig. 15. The interference between d-axis current and q-axis current is caused due to the assumption of linear permeability of the magnetic iron core and the disregard of harmonics of the magnetic flux density in the stator slots air-gap and to an error of measured rotor angle.

The motor produced the smaller torque than the theoretical value as shown in Fig. 14. In terms of this phenomena, an iron loss, especially eddy current loss caused by using solid magnetic soft iron is increased according to be higher speed rotation, and hence, an extra q-axis current to compensate the iron loss should be required in dynamic condition. Therefore the difference between the measured torque and the theoretical value was occurred. There was a constant error between the measured axial attractive force and the theoretical value at every d-axis current as shown in Fig. 15. One of the reasons of the error is accuracy of setting the air-gap length from the rotor surfaces to the top and bottom stators. An eccentricity of the rotor axial position from the set point should generate the biased axial attractive force from the theoretical value.

Operating rotational speed of 4000 rpm is determined using CFD analysis. The hydraulic axial thrust force produced in the pump is 0.14 N at the rotational speed of 4000 rpm. The motor can produce a sufficient electromagnetic force axially to cancel the axial thrust force generated by pumping with rotational speed of 4000 rpm. This result indicates the developed motor has sufficient ability to produce required the axial attractive force and the torque with the vector control algorithm with a steady state operating condition.

Inclinations of the rotor could not be suppressed for rotational speeds over 2500 rpm. These tilting motions caused instability of the rotor in the axial direction and an increase of additional d-axis current to suppress the axial fluctuation of the rotor. The total values of d-axis current and q-axis current is limited and the high speed rotation could not be achieved due to the saturated q-axis current. In order to achieve higher speed rotation, it is necessary to adjust the mass balance of the rotor and to improve the tilt control mechanism of the motor to suppress the tilting motion of the rotor.

5. Conclusion

A double stator axially levitated motor for paediatric VAD has been developed. The developed motor can generate axial force and torque almost independently by using vector control algorithm. The developed motor is successful in levitation and rotation up to a rotational speed of 3000 rpm in the air. This device shows it is possible to achieve smaller size and the experimental results have demonstrated the feasibility of stable levitation and rotation with vector control.

References

[1] H. Onuma, M. Murakami and T. Masuzawa, "Novel maglev pump with a combined magnetic bearing," *ASAIO J.*, Vol. 51, No. 1, pp. 50-55, 2005.

[2] A. Chiba, T. Fukao, O. Ichikawa, M. Oshima, M. Takemoto and D. G. Dorrell, "Magnetic bearings and bearingless drives," *Newnes*, pp. 318-328, 2005.

[3] S. Ueno, T. Okamura, M. Sakagami and S. Tanaka, "Development of miniaturized regenerative pump using axial self-bearing motor," *12th ISMB*, pp. 180-188, 2010.

[4] T. Suzuki, S. Ueno and T. Takeda, "Development of a vacuum pump usin axial-gap self-bearing motor and superconducting magnetic bearing," *12th ISMB*, pp. 733-741, 2010.

[5] T. Masuzawa, S. Ezoe, T. Kato, Y. Okada, "Magnetically suspended centrifugal blood pump with an axially levitated motor," *Artificial Organs*, Vol. 27, Issue 7, pp. 631-638, 2003.

[6] T. Kato, T. Masuzawa and S. Ezoe, "Magnetically levitated rotary artificial heart with axial suspension motor," *8th ISMB*, pp. 9-14, 2002.

[7] N. A. Greatrex, D. L. Timms, E. W. Palmer and T. Masuzawa, "Axial magnetic bearing development for the BiVACOR Rotary BiVAD/TAH," *IEEE Trans. Biomedical Eng.*, Vol. 57, No. 3, pp. 714-721, 2010.

[8] N. Kurita, D. L. Timms, N. Greatrex and T. Masuzawa, "Axial magnetic bearing development for the BIVACOR roary BiBAD/TAH," *11th ISMB*, pp. 217-224, 2008.

[9] S. Ueno and Y. Okada, "Characteristics and control of a bidirectional axial gap combined motor-bearing," *IEEE /Asme Trans. Mechatronics*, Vol. 5, No. 3, pp. 310-318, 2000.

[10] Y. Okada, N. Yamashiro, K, Ohmori and T. Masuzawa, "Mixed flow artificial heart pump with axial self-bearing motor," *IEEE/ASME Trans. Mechatronics*, Vol. 10, pp.658-665, 2005.

[11] Q. D. Nguyen, N. Shimai and S. Ueno, "Control of 6 degrees of freedom salient axial-gap self bearing motor," *12th ISMB*, pp. 627-634, 2010.

[12] J. T. Baldwin, H. S. Borovets, B. W. Duncan, M. J. Gartner, R. K. Jarvik, W. J. Weiss and T. R. Hoke, "The national heart, lung, and blood institute pediatric circulatory support," *J. American heart association*, pp. 147-155, 2006.

[13] B. W. Duncan, "Mechanical circulatory support for infants and children with cardiac disease," *The Annals of Thoracic Surgery*, Vol. 73, pp.1670-1677, 2002.

Creating an ideal "off-test mode" for rotary left ventricular assist devices: Establishing a safe and appropriate weaning protocol after myocardial recovery

Masahiko Ando, MD, PhD,[a,b] Takashi Nishimura, MD, PhD,[c] Yoshiaki Takewa, MD, PhD,[a] Shunei Kyo, MD, PhD,[c] Minoru Ono, MD, PhD,[b] Yoshiyuki Taenaka, MD, PhD,[a] and Eisuke Tatsumi, MD, PhD[a]

Objective: Recent developments in adjunctive therapy have enabled us to remove once-implanted left ventricular assist devices. For successful device removal, appropriate patient selection and precise evaluation of cardiac function are essential. However, with rotary pumps, pump weaning inevitably creates diastolic retrograde pump flow, and this flow may overload the native heart. We developed a novel "off-test mode" for weaning, which increases revolutions per minute just in diastole. The present study evaluated the effect of this mode on retrograde pump flow and ventricular workload.

Methods: The EVAHEART device (Sun Medical Technology Research Corporation, Nagano, Japan) was installed in 8 goats (63.0 ± 7.3 kg). We evaluated myocardial oxygen consumption, pressure volume area, and retrograde pump flow under 3 conditions: circuit clamp, continuous mode, and off-test mode. In continuous mode, revolution per minute was set for a mean net pump flow of zero, whereas in off-test mode, systolic revolution per minute was kept at a minimum level and diastolic revolution per minute was adjusted to ensure near-zero diastolic retrograde pump flow.

Results: In off-test mode, the pressure volume loop shapes were similar to those under circuit-clamp conditions, with both myocardial oxygen consumption and pressure volume area approximately equal to those under clamp conditions. Retrograde pump flow was significantly decreased in off-test compared with continuous mode ($P = .005$).

Conclusions: Off-test mode decreased retrograde flow during weaning while keeping ventricular workload similar to baseline. This mode is potentially valuable for establishing a safe and appropriate pump weaning protocol after myocardial recovery. Investigations on heart failure models are ongoing. (J Thorac Cardiovasc Surg 2012;143:1176-82)

ET/BS

Rotary left ventricular assist devices (LVADs) have greatly improved the outcomes of patients with end-stage heart failure,[1,2] and recent developments in adjunctive therapy have enabled us to remove once-implanted LVADs from more patients than before.[3-5] In the near future, new options, such as stem cell induction[6] or gene therapy,[7] should accelerate myocardial recovery and may further increase the rate of successful LVAD withdrawal.

However, to avoid removal failure, appropriate patient selection and precise evaluation of native heart function are essential.[4,8,9] With pulsatile pumps, which occasionally have extracorporeal pump circuits or mechanical valves to prevent retrograde pump flow (PF), we can clamp the circuits or stop the driving pumps and evaluate cardiac function without support.[10] The judgment should be made promptly, because no PF in the pulsatile system correlates with a high risk of thrombus formation.[8] With rotary pumps, which are widely used at present,[11] circuit clamping is virtually impossible, and taking down pumps inevitably creates a degree of retrograde PF in the diastolic phase, when pressure head (ie, aortic pressure [AoP] – left ventricular [LV] pressure) becomes relatively high. Among the rotary LVADs, axial-flow pumps produce minimal retrograde PF, such that they can be stopped or briefly driven at a low number of revolutions per minute (RPM), allowing a removal decision to be made.[4,11] However, with centrifugal pumps, this decision can be made only by gradually decreasing RPM and carefully establishing low-flow conditions. A mean PF of zero can result in overloading of the native heart and, in the worst case, aggravate its function.[12] Schima and colleagues[10] reported that an assist flow of 1.0 to 1.5 L/min requires work equivalent to that of the unsupported heart in a computer model analysis. However, this condition definitely differs among pump systems, and the optimal weaning protocol for rotary pumps has yet to be established.

From the Department of Artificial Organs,[a] National Cerebral and Cardiovascular Center Research Institute, Department of Cardiothoracic Surgery,[b] and Department of Therapeutic Strategy for Heart Failure,[c] The University of Tokyo, Japan.

Disclosures: Authors have nothing to disclose with regard to commercial support.

Received for publication April 4, 2011; revisions received June 28, 2011; accepted for publication July 26, 2011; available ahead of print Dec 5, 2011.

Address for reprints: Masahiko Ando, MD, PhD, National Cardiovascular Center Research Institute, Department of Artificial Organ, 5-7-1 Fujishiro-dai, Suita, Osaka 565-8565, Japan (E-mail: masandoo@hotmail.com).

0022-5223/$36.00

doi:10.1016/j.jtcvs.2011.07.065

Abbreviations and Acronyms

AoF = aortic flow
AoP = aortic pressure
CVP = central venous pressure
ECG = electrocardiography
EDP = end-diastolic pressure
EDV = end-diastolic volume
ESV = end-systolic volume
LV = left ventricular
LVAD = left ventricular assist device
MVO2 = myocardial oxygen consumption
PF = pump flow
PV = pressure volume
PVA = pressure volume area
RPM = revolutions per minute

Thus, we developed a novel drive mode for centrifugal pumps that can change its RPM in synchronization with heart beats. If we can increase RPM just in diastole, we may be able to control this backward flow. This novel system may help to create the ideal "off-test mode" for a safe and appropriate LVAD weaning protocol. The ideal off-test mode we are suggesting achieves both minimal support in the systolic phase and no forward or backward flow in the diastolic phase. In other words, "zero-total-flow" is created as if circuits are clamped, while keeping the circuits open and pumps driving. We previously reported the effects of this mode on retrograde PF during weaning in mock systems.[12,13] In our experiments, the off-test mode effectively decreased intracircuit retrograde flow in mock circulatory systems. The present study was designed to test this novel system of centrifugal pumps in acute animal models and to evaluate the effects of this mode on retrograde PF and LV workload, or myocardial oxygen consumption (MVO2) and pressure volume area (PVA).

MATERIALS AND METHODS

Experimental Preparation

Experiments were performed on 8 goats (63.0 ± 7.3 kg) sedated with an intramuscular injection of ketamine (10 mg/kg). General anesthesia was maintained by inhalation of isoflurane. The animals were fixed in the right recumbent position and mechanically ventilated. Inhaled oxygen was controlled to achieve a target arterial oxygen pressure of 100 to 150 mm Hg. The heart was approached via a left thoracotomy, and pressure lines for AoP and central venous pressure (CVP) monitoring were established from the left internal thoracic artery and vein. We placed an 18-mm electromagnetic flow probe (EMF-1000, Nihon Kohden, Tokyo, Japan) on the ascending aorta for ascending aortic flow (AoF) monitoring and a 3-mm ultrasonic flow probe (HQD3FSB, Transonic Systems Inc, New York, NY) on the main trunk of the left coronary artery for coronary flow monitoring. A 16-mm outflow cannula was sutured to the descending aorta, and a 16-mm ultrasonic flow probe (TS420, Transonic Systems Inc) was placed around the outflow cannula for PF monitoring. After heparinization (300 U/kg), the LV apex was removed with a 19-mm puncher, and a 20-mm inflow cannula was inserted. Both outflow and inflow cannulae were connected to the EVAHEART device (Sun Medical Technology Research Corporation, Nagano, Japan),[14] and left heart bypass was started. A 4F Mikro-Tip catheter pressure transducer (Millar Instruments, Houston, Tex) and 6F conductance catheter (2S-RH-6DA-116, 6F, 6 mm, Taisho Biomed Instrument Co, Ltd, Osaka, Japan) were inserted from the anterior wall of the LV for pressure volume (PV) loop monitoring. The inferior vena cava was encircled for preload reduction to obtain an end-systolic PV relationship. A pacing lead for detection of ventricular electrocardiography (ECG) was sutured on the anterior wall of the right ventricle (Figure 1, *A*).

After these preparations, we waited for at least 30 minutes to ensure hemodynamic stability. All experimental protocols were approved by the Animal Research Committee of the National Cerebral and Cardiovascular Center Research Institute and conducted according to its veterinary guidelines.

Experimental Protocol

During data collection, target preload was set at 10 mm Hg by mean CVP, and we controlled the infusion volume to maintain this level. Target heart rate and systolic pressure were 60 to 90 beats/min and 80 to 120 mm Hg, respectively. If these parameters deviated from their targets, we adjusted the concentration of inhaled isoflurane. No vasopressive agents were used. Lidocaine (1 mg/kg/h) was continuously infused to prevent ventricular arrhythmias. We evaluated retrograde PF and LV workload under 3 conditions: 1) circuit clamp (no pump support), 2) continuous mode (constant RPM), and 3) off-test mode (increasing RPM in diastole). RPM settings for these modes are described in detail below. We waited 5 minutes to obtain hemodynamic stability after setting up the drive mode. Pressure and flow data were collected in Labchart5 (ADInstruments Pty Ltd, Bella Vista, Australia). We analyzed PF waveforms. Negative PF was integrated by time, and retrograde PF was calculated and shown as the amount per minute. At completion of the experiments, the hearts were excised, and the LV was weighed for weight normalization of MVO2 and PVA per 100 grams of LV tissue.

Drive Mode

In continuous mode, RPM was set to establish a mean PF of approximately 0 L/min. In off-test mode, we used the following novel ECG-synchronized RPM change mode. Direct ECG detection from a ventricular lead for synchronization in pulsatile LVADs was previously reported,[15] but direct ECG-synchronized RPM change for rotary LVADs is rare according to our search of the literature, and we are currently developing various clinical applications for this system.[16,17]

The details of our novel pump controller have been reported.[13] Briefly, the controller can detect R waves from the ventricular ECG and instantly increase RPM to the target speed after configuration of the delay time from the R wave. The primary goal of our off-test mode is achieving both minimal systolic support and prevention of diastolic retrograde PF. Therefore in off-test mode, systolic RPM was set at 700, which is the minimum RPM of the current system, and diastolic RPM was set to ensure diastolic PF near 0 L/min. We adjusted this diastolic RPM manually while monitoring the PF curve. The time that the target speed is maintained can also be configured. We defined the systolic phase as 33% of the RR interval and the diastolic phase as the remaining 67%. Thus, in off-test mode, delay time was set as the systolic phase, or 33% of the RR interval. For example, at a native heart rate of 90 beats/min, the RR interval is 670 msec, with 33% being 220 msec. Pumps were thus driven at a systolic RPM of 700 from the R-wave input for 220 msec, and diastolic RPM was instantly increased to achieve a diastolic PF of approximately 0 L/min. We maintained this diastolic RPM for the other 67% of the RR interval, or 450 msec, and finally returned to the initial systolic RPM of 700 rpm. We calculated the bypass rate by dividing PF by the sum of PF and AoF, as shown in "Results."